Supporting Information

Identification of Degree of Ordering in Spinel $LiNi_{0.5}Mn_{1.5}O_4$ through NMR and Raman Spectroscopies supported by Theoretical Calculations

Gozde Oney[#1,2,3], Jon Serrano Sevillano[#1,4,5], Mouna Ben Yahia[3,6], Jacob Olchowka[1,3,5], Emmanuelle Suard[7], Francois Weill[1,3], Arnaud Demortière[2,3,5], Montse Casas Cabanas[4,5,8], Laurence Croguennec[1,3,5]* and Dany Carlier[1,3,5]*

[1] CNRS, Univ. Bordeaux, Bordeaux INP, ICMCB UMR 5026, F-33600 Pessac, France

[2] Laboratoire de Réactivité et de Chimie des Solides (LRCS), CNRS-UPJV UMR 7314, F-80039 Amiens Cedex 1, France

[3] RS2E, Réseau Français sur le Stockage Electrochimique de l'Energie, FR CNRS 3459, F-80039 Amiens Cedex 1, France

[4] Centro de Investigación Cooperativa de Energías Alternativas (CIC energiGUNE), Basque Research and Technology Alliance (BRTA), Parque Tecnológico de Álava, Albert Einstein 48, 01510 Vitoria-Gasteiz, España.

[5] ALISTORE-ERI European Research Institute, FR CNRS 3104, F-80039 Amiens Cedex 1, France

[6] ICGM, University of Montpellier, CNRS, ENSCM, Montpellier, France

[7] Institut Laue-Langevin (ILL), BP 156, 71 Avenue des Martyrs, 38042 Grenoble, France

[8] Ikerbasque - Basque Foundation for Science, Euskadi Pl., 5, 48009 Bilbao, Spain

[#] equal contributions

*Corresponding authors: laurence.croguennec@icmcb.cnrs.fr

dany.carlier@icmcb.cnrs.fr

Table S1: ICP-OES analysis of disordered and ordered LNMO samples

	Li/M	**Mn/M**	**Ni/M**
Expected	*0.50*	*0.75*	*0.25*
***d* - LNMO**	0.50 ± *0.02*	0.77 ± *0.04*	0.23 ± *0.02*
***o* - LNMO**	0.47 ± *0.02*	0.76 ± *0.04*	0.24 ± *0.02*

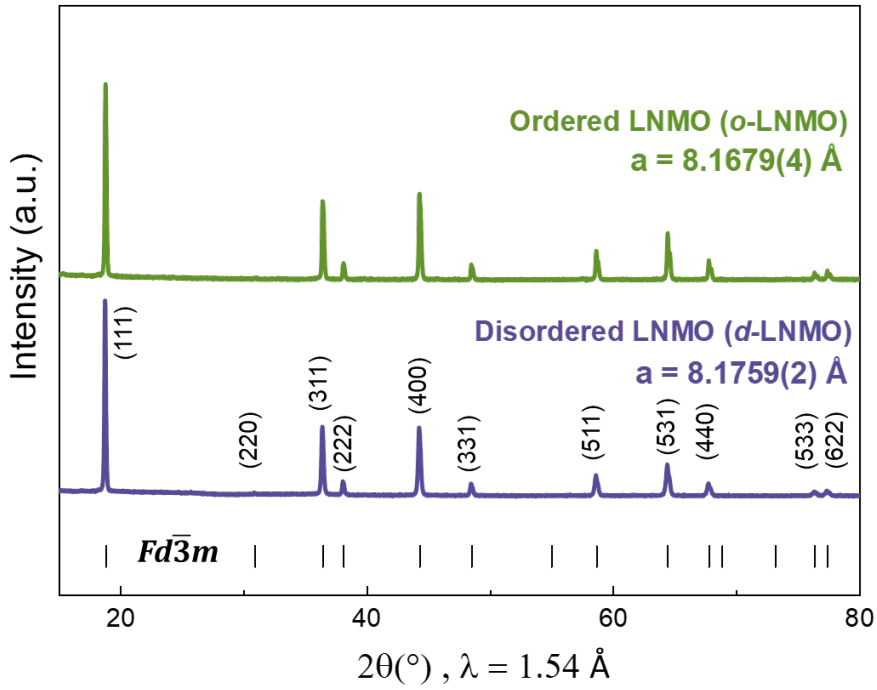

Figure S1: Powder X-Ray diffraction patterns of the synthesized disordered and ordered LNMO showing characteristic peaks of spinel, indexed within $Fd\bar{3}m$ space group.

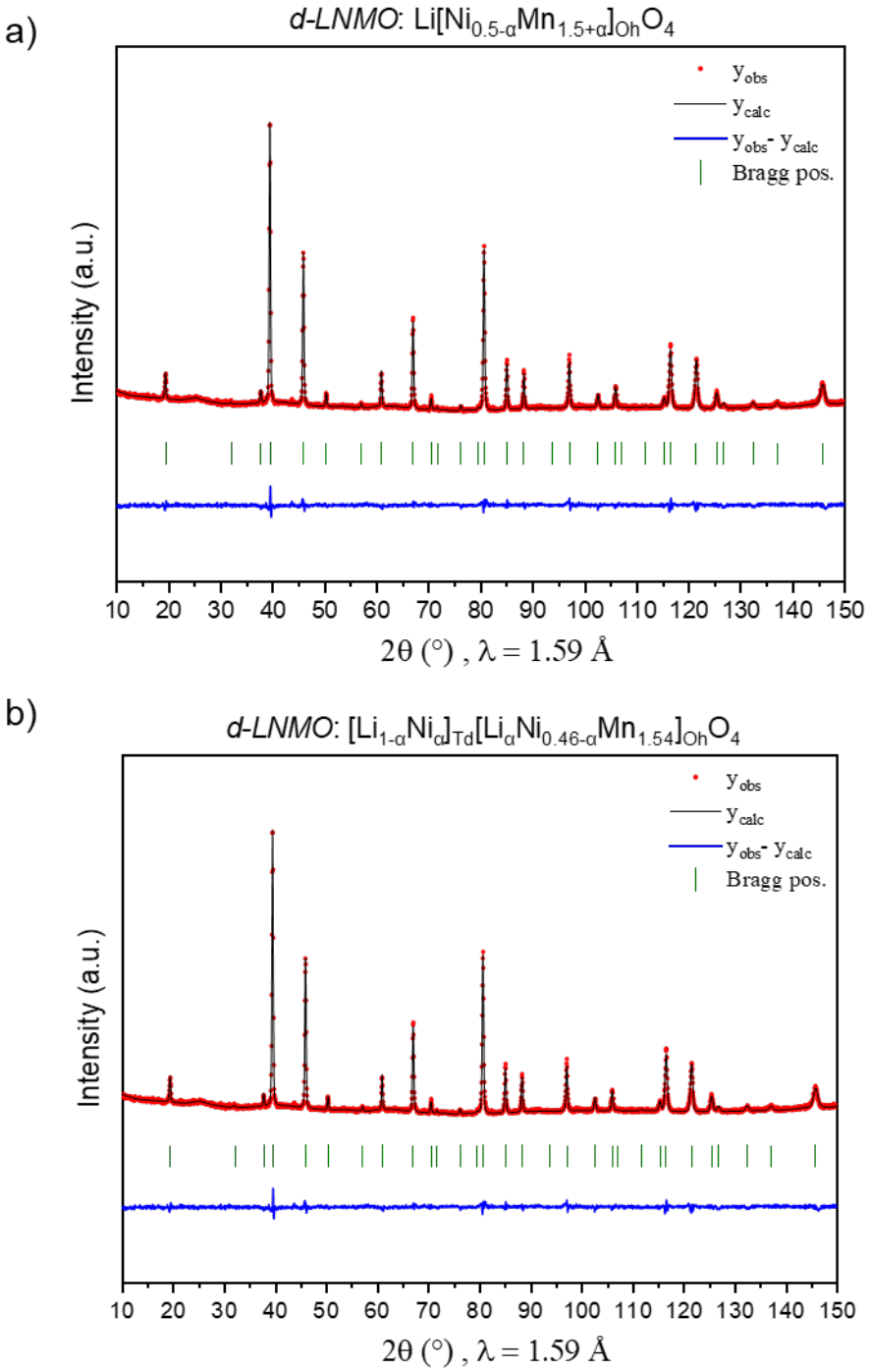

Figure S2: Rietveld fits of the neutron powder diffraction pattern collected for *d*-LNMO in the unit cell described in the *Fd-3m* space group. a) Conventional description, with Ni and Mn atoms occupying *16d* octahedral site, the Ni/Mn ratio is evaluated; b) An exchange between Li and Ni atoms on *8a* tetrahedral and *16d* octahedral sites was considered.

Table S2: Rietveld results obtained for *d*-LNMO considering two different models: In the first, the sites' occupancies were evaluated according to the theoretical distribution of Li in the 8*a* tetrahedral site and Ni/Mn in the 16*d* octahedral site; for comparison, in the second model, a Li/Ni exchange was considered between the tetrahedral and octahedral sites. The atomic displacement parameters of transition metals could not be refined simultaneously with their occupancies, thus, were kept fixed.

d-LNMO : $Li_1[Ni_{0.5-\alpha}Mn_{1.5+\alpha}]_{Oh}O_4$

Space Group : *Fd*-3*m* (227) , a = 8.1759(2) Å

Atom	Wyckoff	x	y	z	Occ.	B_{iso}, Å^2
Li	8*a*	1/8	1/8	1/8	1	1.3(2)
Mn	16*d*	1/2	1/2	1/2	0.769(2)	0.6
Ni	16*d*	1/2	1/2	1/2	0.231(2)	0.6
O	32*e*	0.2630(1)	0.2630(1)	0.2630(1)	1	0.9(4)

Agreement Factors: R_p = 26.9%, R_{wp} = 16.9%, R_B = 9.5%, χ^2 = 1.95

d-LNMO : $[Li_{1-\alpha}Ni_\alpha]_{Td}[Li_\alpha Ni_{0.46-\alpha}Mn_{1.54}]_{Oh}O_4$

Space Group : *Fd*-3*m* (227) , a = 8.1759(2) Å

Atom	Wyckoff	x	y	z	Occ.	B_{iso}, Å^2
Li1	8*a*	1/8	1/8	1/8	0.999(2)	1.3(2)
Ni2	8*a*	1/8	1/8	1/8	0.001(2)	1.3(2)
Mn	16*d*	1/2	1/2	1/2	0.77	0.6
Ni1	16*d*	1/2	1/2	1/2	0.229(2)	0.6
Li2	16*d*	1/2	1/2	1/2	0.001(2)	0.6
O	32*e*	0.2630(1)	0.2630(1)	0.2630(1)	1	0.9(4)

Agreement Factors: R_p = 26.6%, R_{wp} = 16.8%, R_B = 9.54%, χ^2 = 1.92

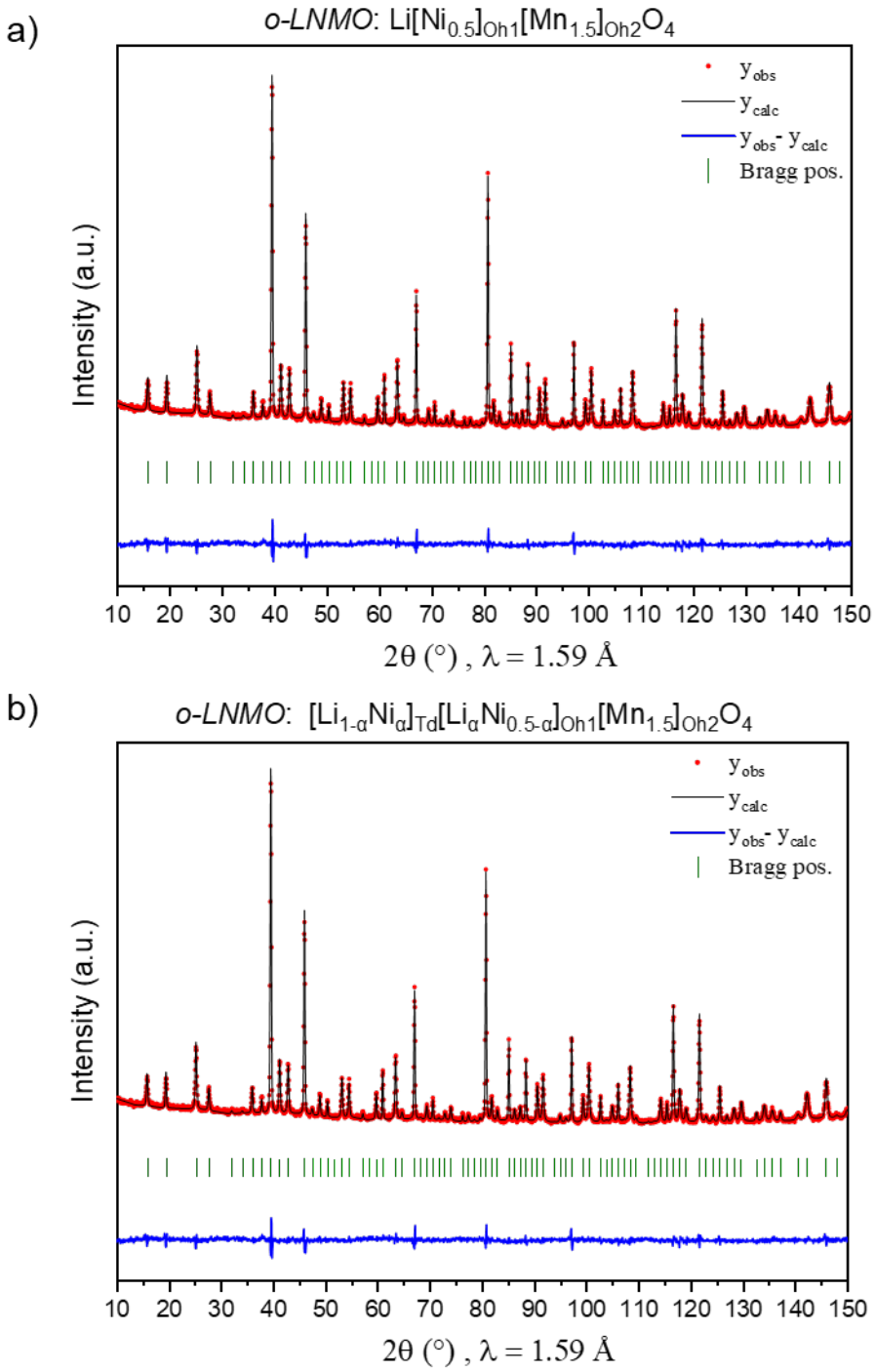

Figure S3: Rietveld fits of the neutron powder diffraction pattern collected for *o*-LNMO. a) Conventional description in the $P4_332$ space group, with Ni atoms in 4*b* and Mn atoms in 12*d* octahedral sites; b) An exchange between Li and Ni atoms sitting on 8*c* tetrahedral and 4*b* octahedral sites was considered.

Table S3: Rietveld results obtained for *o*-LNMO considering two different models: In the first, the sites' occupancies were fixed according to the theoretical distribution of Li in the 8*c* tetrahedral site and Ni in the 4*b* octahedral site; for comparison, in the second model, a Li/Ni exchange was considered between the tetrahedral and octahedral sites.

o-LNMO : $Li_1[Ni_{0.5}]_{Oh1}[Mn_{1.5}]_{Oh2}O_4$

Space Group : $P4_332$ (212) , a = 8.1679(4) Å

Atom	Wyckoff	x	y	z	Occ.	B_{iso}, Å^2
Li	8*c*	0.003(2)	0.003(2)	0.003(2)	1	0.8(2)
Mn	12*d*	1/8	0.3788(8)	-0.1288(8)	1	0.3(6)
Ni	4*b*	5/8	5/8	5/8	1	0.5(4)
O1	8*c*	0.3842(4)	0.3842(4)	0.3842(4)	1	0.4(2)
O2	24*e*	0.1503(4)	-0.1422(4)	0.1242(4)	1	0.4(2)

Agreement Factors: R_p = 17.7%, R_{wp} = 14.7%, R_B = 7.63%, χ^2 = 2.35

o-LNMO : $[Li_{1-\alpha}Ni_\alpha]_{Td}[Li_\alpha Ni_{0.5-\alpha}]_{Oh1}[Mn_{1.5}]_{Oh2}O_4$

Space Group : $P4_332$ (212) , a = 8.1679(4) Å

Atom	Wyckoff	x	y	z	Occ.	B_{iso}, Å^2
Li1	8*c*	0.003(2)	0.003(2)	0.003(2)	0.994(4)	0.7(2)
Ni2	8*c*	0.003(2)	0.003(2)	0.003(2)	0.006(4)	0.7(2)
Mn	12*d*	1/8	0.125	0.125	1	0.3(6)
Ni1	4*b*	5/8	5/8	5/8	0.988(4)	0.4(6)
Li2	4*b*	5/8	5/8	5/8	0.012(4)	0.4(6)
O1	8*c*	0.3842(4)	0.3842(4)	0.3842(4)	1	0.4(4)
O2	24*e*	0.1503(4)	-0.1422(4)	0.1242(4)	1	0.4(4)

Agreement Factors: R_p = 17.7%, R_{wp} = 14.7%, R_B = 7.82%, χ^2 = 2.35

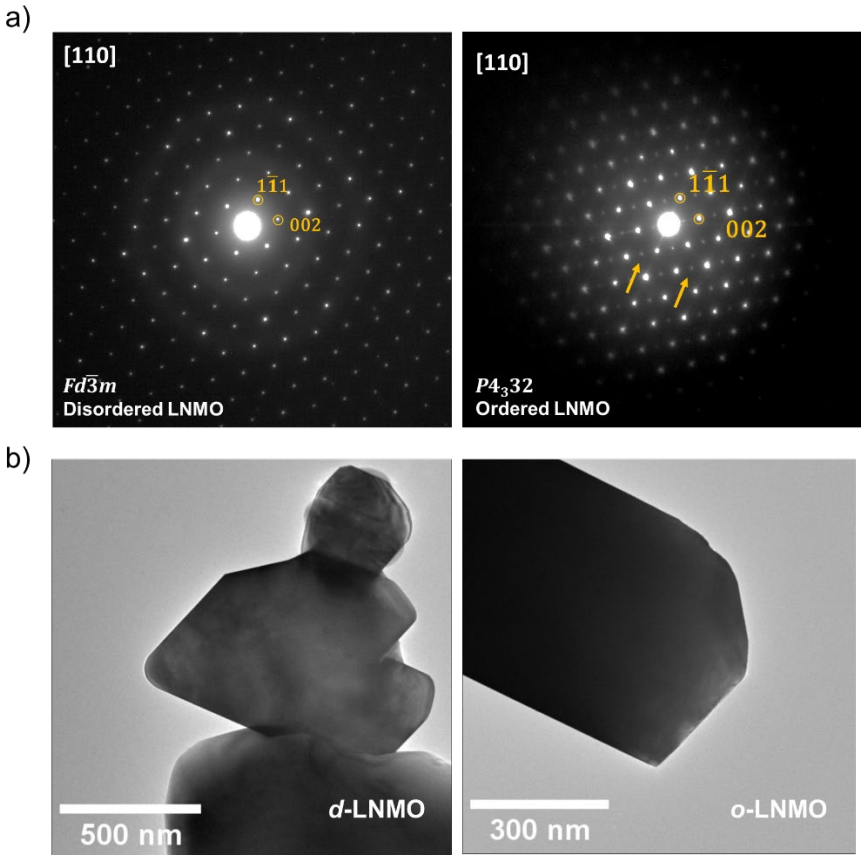

Figure S4: (a) Electron diffraction patterns (SAED) at [110] zone axis and associated TEM images for *d*-LNMO (left) and *o*-LNMO (right) samples, orange arrows highlight representative ordering spots in SAED pattern of *o*-LNMO. (b) Associated TEM images of *d*- and *o*-LNMO (left to right). At least 20 particles were analyzed for each sample, agreeing with the lattice description of a disordered and ordered spinel, respectively, for *d*- and *o*-LNMO.

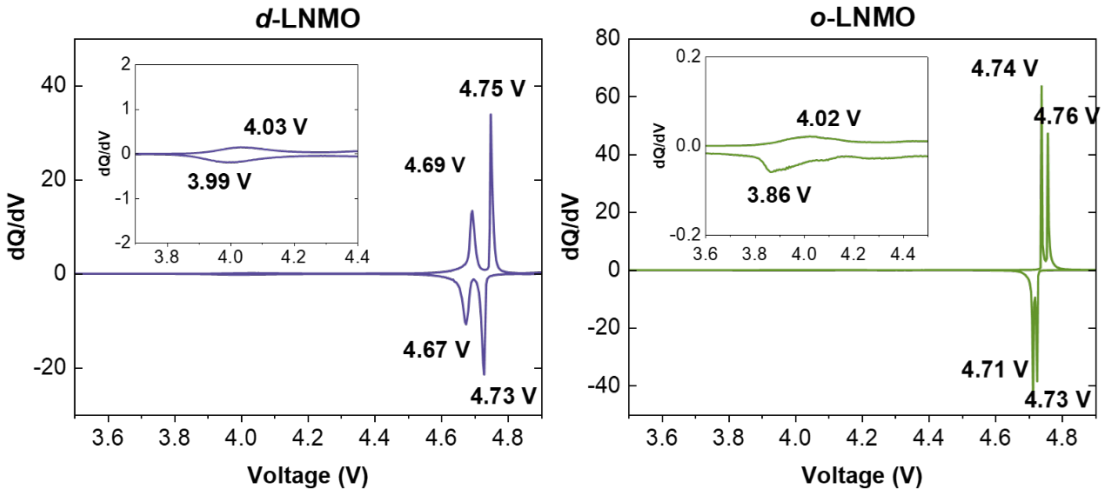

Figure S5: dQ/dV derivative curves calculated for *d*-LNMO and *o*-LNMO samples and corresponding to the 2nd cycle performed at C/10 rate.

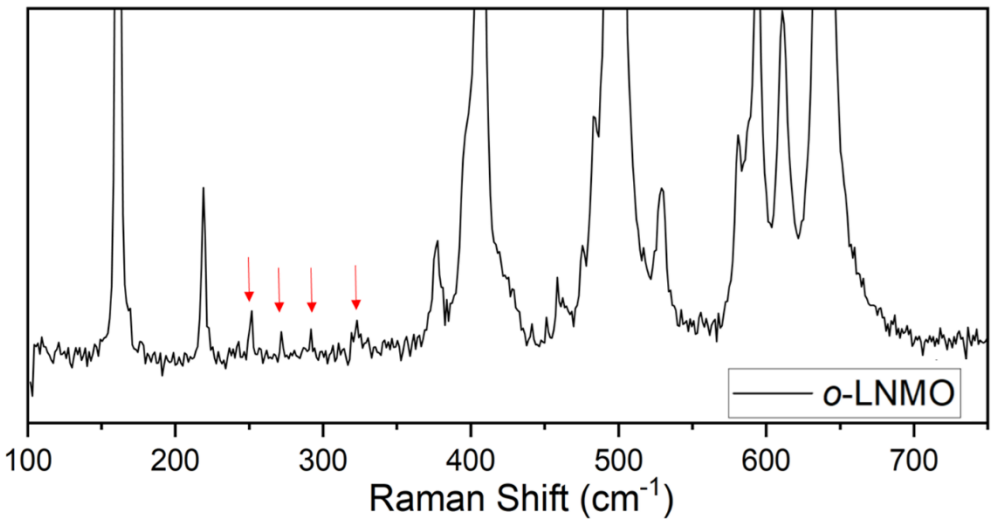

Figure S6: Enlarged Raman spectrum of *o*-LNMO. The arrows indicate a set of small intensity peaks as an example.

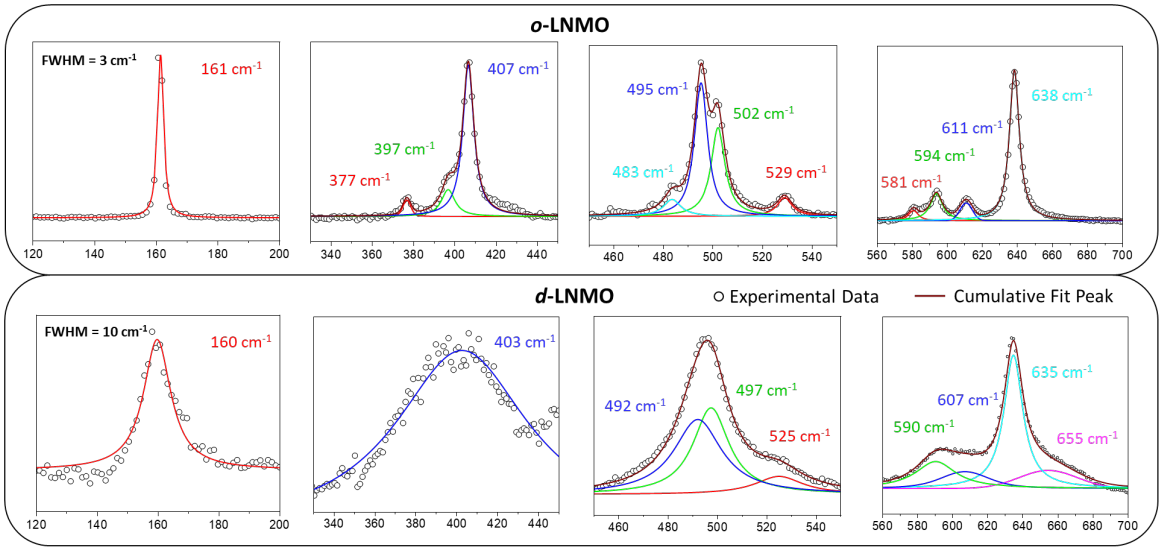

Figure S7: Comparison of selected Raman deconvoluted bands for the two LNMO samples. The full width at half-maximum values are given for the observed single peak at ~160 cm^{-1} in both samples. A FWHM of 3 cm^{-1} demonstrates extended crystalline domains for *o*-LNMO while the broadening (FWHM of 10 cm^{-1}) for *d*-LNMO is caused by transition metal disorder in spinel and thus defects that limit the size of the crystalline domains.

Table S4: Attribution of the Raman bands based on the decomposition of the experimental spectra of *d*-LNMO ($Fd\bar{3}m$ s.g.) and *o*-LNMO ($P4_332$ s.g.). For *d*-LNMO, the number of active modes does not correspond to the theoretically predicted active modes for the structure because of the Mn mixed valence and the global disorder in the structure. The mode at 655 cm^{-1} is also generated by the Mn^{3+} presence, thus is not attributed in $Fd\bar{3}m$ lattice symmetry. For *o*-LNMO, since the number of decomposed modes is less than predicted by the $P4_332$ space group, only the highest intensities were attributed.

d-LNMO		*o*-LNMO	
Position	Symmetry	Position	Symmetry
160	F_{2g}	161	A_1
403	E_g	377	E
492	--	397	F_2
497	F_{2g}	407	E
525	--	483	A_1
590	--	495	A_1
607	F_{2g}	502	A_1
635	A_{1g}	529	F_2
655	--	581	E
		594	A_1/F_2
		611	F_2
		638	A_1

More information on theoretical calculations performed for Raman Spectroscopy

We must emphasize that our attempts to model the Raman spectrum using other functionals such as PBE, PBE0, and HSE06 have failed, resulting in aberrant refractive index values and Born charges. While in the case of B3LYP, the calculated refractive index of *o*-LNMO is about 2.3 in the three directions. As far as we know, no experimental values were reported in the literature to enable a comparison. Nevertheless, this value is close to that reported for $LiMn_2O_4$ spinel (2.7)[1]

For defect-containing ordered spinels, we have considered the following hypothetical structures with y=0.125:

(1) $(Li_{1-y}Ni^{2+}{}_y)_{Td}(Li_yNi^{2+}{}_{0.5-y})_{Oh1}(Mn^{4+}{}_{1.5})_{Oh2}O_4$,

(2) $(Li_{1-y}Mn^{4+}{}_y)_{Td}(Ni^{2+}{}_{0.5})_{Oh1}(Li_yMn^{4+}{}_{1.5-y})_{Oh2}O_4$

(3) $(Li_1)_{Td}(Mn_yNi^{2+}{}_{0.5-y})_{Oh1}(Ni^{2+}{}_yMn^{4+}{}_{1.5-y})_{Oh2}O_4$

Table S5: Calculated free energies and the associated structural parameters determined for each model. For all the different models considered, the calculated free energies at 298 K are reported in reference to the ordered phase. Positive energy values indicate that the respective model is less stable than the *o*-LNMO.

Model	Free Energy (eV) (E_{ref}-E_i)	Cell param. Å	d(Li-O) Å	d(Mn-O) Å	d(Ni-O) Å	Born charge
o-LNMO (ref)	0	8.255	1.97-2.00	1.89-1.95	2.08	Mn : 4.04 Ni : 2.12
Li/Mn (8*c*/12*d*)	0.347	8.240	$[1.95\text{-}2.04]_{Td}$ $[2.08\text{-}2.14]_{Oh}$	$[1.86\text{-}2.04]_{Td}$ $[1.86\text{-}1.96]_{Oh}$	$[1.89\text{-}2.09]_{Oh}$	Mn_{Td} : 2.37 Mn_{Oh} : 4.05 Ni : 1.99
Li/Ni (8*c*/4*b*)	0.163	8.255	$[1.96\text{-}2.00]_{Td}$ $[2.10]_{Oh}$	$[1.85\text{-}2.10]_{Oh}$	$[1.96\text{-}2.00]_{Td}$ $[2.06\text{-}2.09]_{Oh}$	Mn_{Oh} : 3.99 Ni_{Td} : 2.38 Ni_{Oh} : 1.99
Ni/Mn (4*b*/12*d*)	0.337	8.281	1.95-2.004	1.89-1.95	$[1.89\text{-}2.09]_{Oh}$	Mn : 3.46 ;4.04 Ni : 2.43 ; 2.01

Table S6: The wavenumbers, in cm^{-1}, of the most pertinent normal modes of the *o*-LNMO, Li/Ni, and Li/Mn antisite defect models. The frequencies in bold correspond to the evolution of the predominant mode in the *o*-LNMO phase depending on the nature of the defects. Notably, the presence of a Li/Mn defect induces a minor splitting of this mode.

o-LNMO	Li/Ni defect	Li/Mn defect
650	**675**	**656**
640	643	**654**
616	627	650
570	643	629
508	627	628
477	623	612
402	610	609
390	580	603
370		598
225		582
171		549
		531

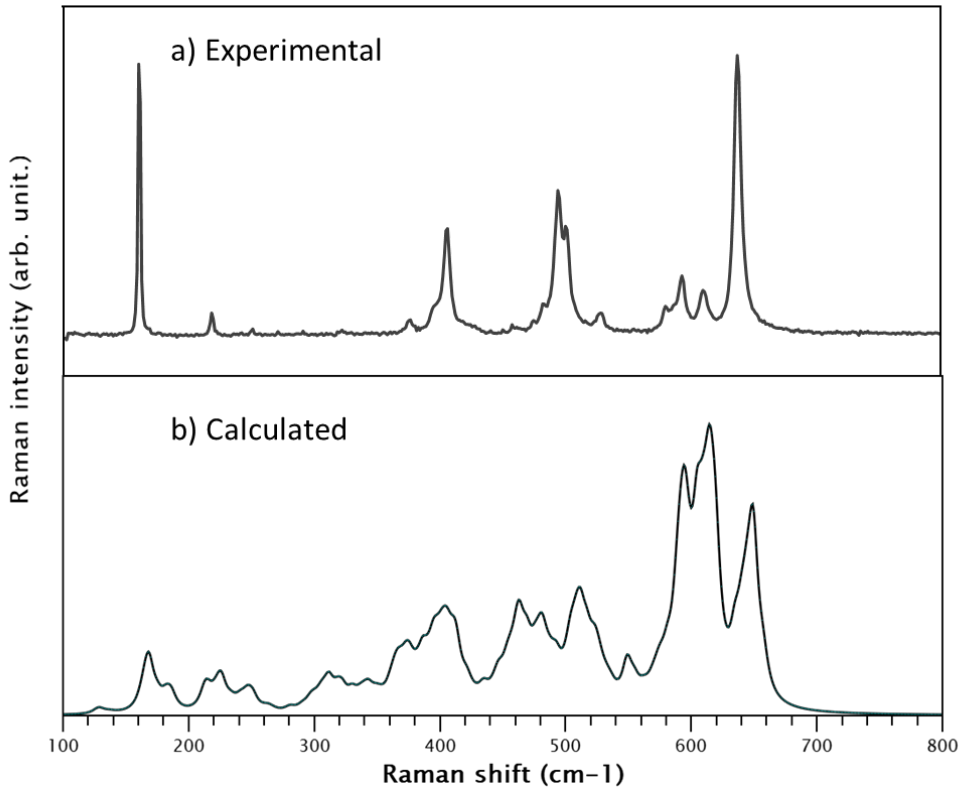

Figure S8: (a) Comparison of the experimental Raman spectrum and (b) the calculated spectrum for the hypothetical model considering a Ni/Mn exchange in *o* LNMO (Oh1/Oh2) showing major alterations compared to the expected spectra.

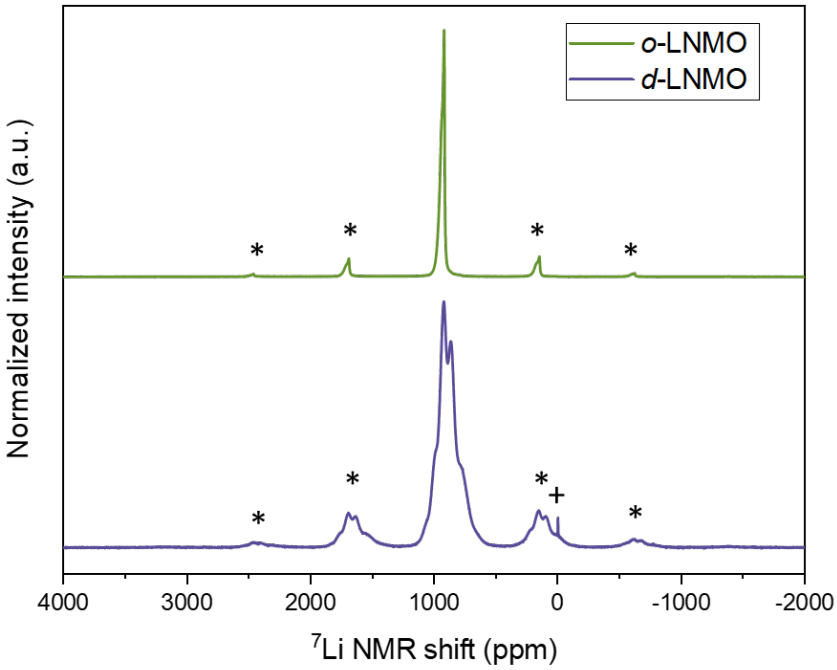

Figure S9: Full ^{7}Li solid-state MAS NMR spectra recorded for LNMO samples. The symbols * allow identifying the spinning sidebands, while the symbol + highlights the presence of a small amount of Li contained in a diamagnetic impurity.

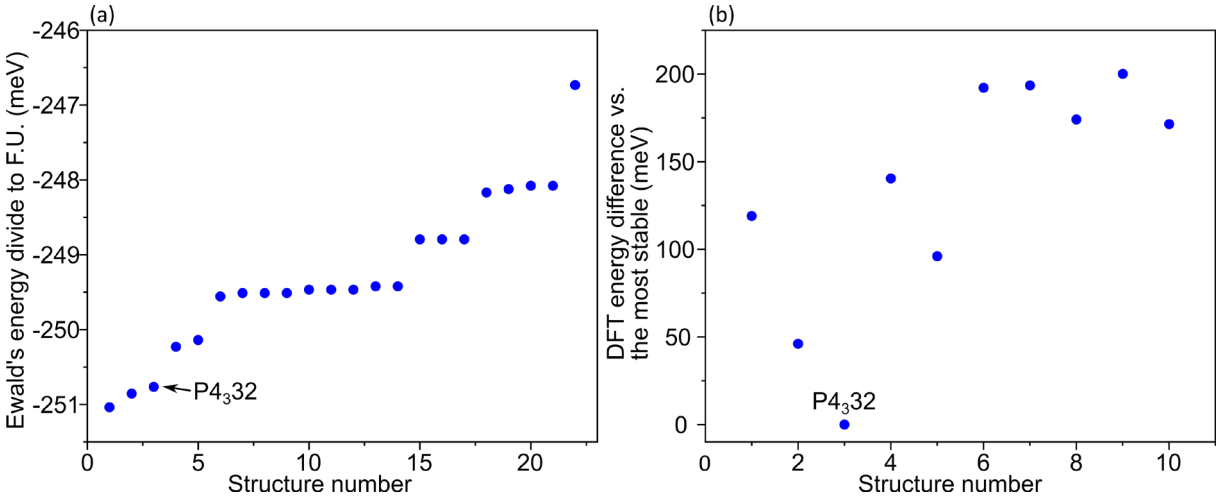

Figure S10: (a) Ewald's electrostatic energy normalized by formula unit, calculated for the 23 structures with different Mn/Ni ordering. (b) Calculated DFT energy normalized by formula unit of the most stable configurations in (a).

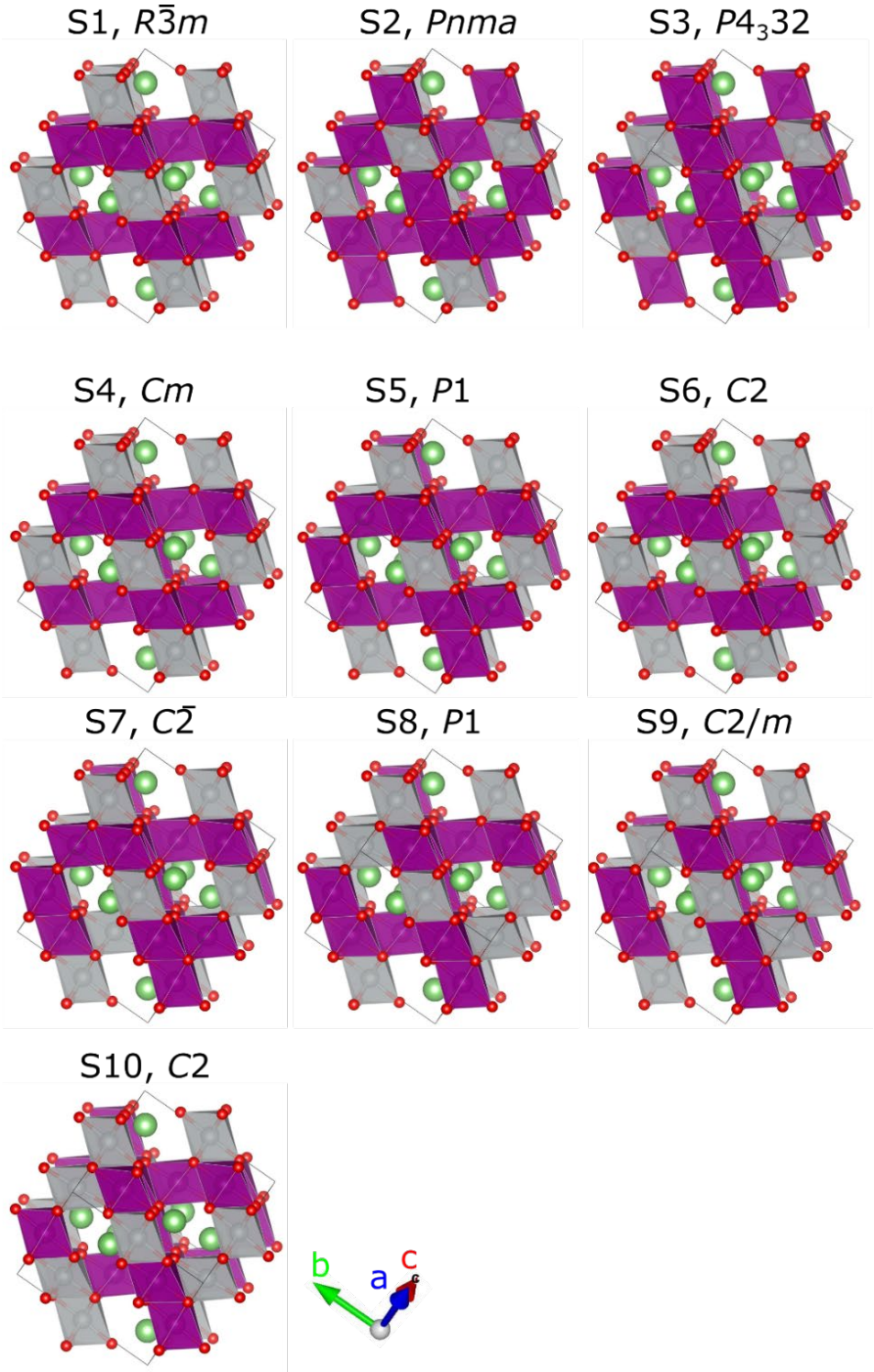

Figure S11: 10 most stable configurations according to Ewald's energy for which the DFT energy is calculated.

Table S7: Calculated chemical shift values for the lithium atoms coming from the hyperfine coupling parameter. The local environment of each lithium is highlighted in the last column.

Structure	**Atom**	***Chemical shift***	***Local environment***
S3 (ideal)	8xLi	960	Ideal structure
S5 (disordered)	Li	*1122.8*	Ni-rich
	Li	*1072.9*	*$MnNi_2$ config.*
	Li	*865.0*	Ideal in disordered
	Li	*1048.0*	*$MnNi_2$ config.*
	Li	*740.2*	*Mn-rich*
	Li	*873.3*	Ideal in disordered
	Li	*831.7*	Ideal in disordered
	Li	*898.3*	Ideal in disordered

References:

1. Cazorla Soult, M. *et al.* Spectroscopic Ellipsometry for Operando Monitoring of (De)Lithiation-Induced Phenomena on $LiMn_2O_4$ and $LiNi_{0.5}Mn_{1.5}O_4$ Electrodes. *J. Electrochem. Soc.* **169**, 040501 (2022).